

Drivers of the evolution and amplitude of African Humid Periods

Laurie Menviel ^{1✉}, Aline Govin ², Arthur Avenas ^{1,3,4}, Katrin J. Meissner ^{1,3}, Katharine M. Grant ⁵ & Polychronis C. Tzedakis ⁶

During orbital precession minima, the Sahara was humid and more vegetated, providing potential corridors for Hominins migration. Uncertainties remain over the climatic processes controlling the initiation, demise and amplitude of these African Humid Periods. Here we study these processes using a series of transient simulations of the penultimate deglaciation and Last Interglacial period, and compare the results with a transient simulation of the last deglaciation and Holocene. We find that the strengthening of the Atlantic Meridional Overturning Circulation at the end of deglacial millennial-scale events exerts a dominant control on the abrupt initiation of African Humid Periods as the Atlantic Meridional Overturning Circulation modulates the position of the Intertropical Convergence Zone. In addition, residual Northern Hemispheric ice-sheets can delay the peak of the African Humid Period. Through its impact on Northern Hemispheric ice-sheets disintegration and thus Atlantic Meridional Overturning Circulation, the larger rate of insolation increase during the penultimate compared to the last deglaciation can explain the earlier and more abrupt onset of the African Humid Period during the Last Interglacial period. Finally, we show that the mean climate state modulates precipitation variability, with higher variability under wetter background conditions.

¹Climate Change Research Centre, University of New South Wales, Sydney, Australia. ²Laboratoire des Sciences du Climat et de l'Environnement (LSCE), Institut Pierre Simon Laplace (IPSL), CEA-CNRS-UVSQ, Université Paris-Saclay, Gif-Sur-Yvette 91190, France. ³ARC Centre of Excellence for Climate Extremes, University of New South Wales, Sydney, Australia. ⁴École Polytechnique, Palaiseau, France. ⁵Research School of Earth Sciences, Australian National University, Canberra, Australia. ⁶Environmental Change Research Centre, Department of Geography, University College London, London, UK. ✉email: l.menviel@unsw.edu.au

The climate of tropical north Africa is under the influence of the West African monsoon (WAM), which is characterised by a low-level southwesterly flow bringing moist air from the equatorial Atlantic towards the Saharan heat low during boreal summer¹. The WAM is associated with the position of the Intertropical Convergence Zone (ITCZ), which lies at the convergence of the southwesterly monsoon flow and the dry north-easterly Harmattan winds. The ITCZ, here identified as the latitude of maximum precipitation, is located at the energy flux equator², and its position is thus linked to the atmospheric energy transport and the meridional temperature gradient. The African Easterly Jet (AEJ) is maintained by meridional surface temperature and soil moisture gradients over tropical north Africa^{3,4}, but also arises from the meridional circulations controlled by the ITCZ to the south and Saharan heat low to the north⁵. Both the ITCZ and the AEJ modulate present-day precipitation over the Sahel (14°N–18°N), with a weak and northward displaced AEJ leading to wet conditions^{1,6}. However, changes in background conditions will impact the positions of the ITCZ and AEJ and thus precipitation over tropical north Africa.

As a result of the low precession and associated high boreal summer insolation prevailing during the early Holocene, the ITCZ was located further north during summer, thus leading to wetter conditions over the Sahel and Sahara. During this African Humid Period (AHP, ~11–5.5 thousand years before present, thereafter ka) the Sahara had increased vegetation cover and biodiversity, including tropical plant species⁷, and an extensive network of drainage channels and lakes⁸.

The AHP was not restricted to the Holocene but occurred during previous periods of high boreal summer insolation, in phase with precession minima^{9–13}. During the Last Interglacial period (LIG, ~129–116 ka), the warmest interglacial period of the last 800 ka¹⁴, summer insolation at high northern latitudes was more than 70 W/m² higher than during the pre-industrial (PI). As a result, North Atlantic marine records suggest that summer sea surface temperatures (SSTs) were 1.1 to 1.9 °C higher than PI^{15,16}. The greater summer insolation in the Northern Hemisphere (NH) at the LIG most likely shifted the ITCZ northward, thus leading to wetter conditions over tropical north Africa¹⁷. Paleo-proxy records from tropical north Africa indeed suggest wetter conditions and a likely northward expansion of trees between ~127 and 122 ka^{13,18–20}. Deposition of organic-rich layers in the Mediterranean Sea (sapropels), also suggests increased monsoon runoff from tropical north Africa during the LIG^{9,21,22}.

Time slice numerical simulations of the mid-Holocene (6 ka) and LIG (127 ka) consistently highlight a larger areal extent and stronger WAM during these time periods compared to PI¹⁷, although these simulations could underestimate both the amplitude and extent of the AHP because they did not account for vegetation-climate feedbacks^{23–25}. While the time evolution of precipitation over tropical north Africa during the last glacial-interglacial cycle was previously simulated^{13,26}, millennial-scale variability was not included and the processes leading to the onset and demise of the AHPs during the last two interglacials were not studied in detail. In addition, sapropel records covering the last 150 ka have shown that there is no constant relationship between insolation maxima and sapropel mid-points, suggesting that the timing of sapropel depositions, and thus AHPs, could also be linked to ice-volume/meltwater changes occurring during the preceding deglaciation²².

Both the penultimate (~140–129 ka) and last (~18–10 ka) deglaciations featured millennial-scale climatic events, during which the Atlantic Meridional Overturning Circulation (AMOC) weakened: Heinrich stadial 11 (HS11, main phase at ~133.3–128.5 ka), Heinrich stadial 1 (~18–14.7 ka) and the

Younger Dryas (~12.8–11.7 ka)^{27–29}. Through its modulation of meridional ocean heat transport, the strength of the AMOC can impact the location of the ITCZ and thus precipitation patterns over tropical north Africa^{30–32}. The impact of deglacial changes in insolation and follow-on processes in the climate system on the AHP initiation thus needs to be better constrained.

Finally, paleo-proxy records suggest that the AHP termination during the mid-Holocene was locally abrupt in contrast to the slow insolation decrease^{24,33}. As such, it has been hypothesised that the abrupt AHP demise could have arisen from vegetation or dust feedbacks. The broad time-transgressive end of the AHP was recently simulated in a transient experiment of the Holocene due to the different regional controls on precipitation³⁴. In contrast, the end of the AHP during the LIG has received little attention. Comparing the AHP evolution across the two interglacials can shed light onto the processes controlling its amplitude and timing.

Here, we study the evolution of precipitation and vegetation cover over tropical north Africa across the penultimate deglaciation and the LIG, and analyse the drivers of precipitation changes as simulated by a suite of transient simulations performed with an Earth system model. The simulated precipitation evolution across the period 140 to 120 ka is further compared to a transient simulation covering the last deglaciation and Holocene (18–3 ka) performed with the same Earth system model, as well as to selected paleo-records.

Results

Climatic changes across the penultimate deglaciation and the LIG. The transient simulation of the penultimate deglaciation (*Full*, Methods) is performed with the Earth system model LOVECLIM³⁵, and is forced by changes in orbital parameters³⁶, greenhouse gases³⁷, ice-sheet topography and associated albedo, as well as meltwater input in the North Atlantic following the PMIP4 protocol³⁸ (Methods). As boreal summer insolation and greenhouse gases increase across the deglaciation (Fig. 1a, b), simulated air temperature increases over Antarctica by 12.4 °C between 136.8 and 128 ka, in agreement with the EPICA Dome C ice core³⁹ (Fig. 1d). Across the deglaciation, SSTs off the Iberian margin increase by up to 7.2 °C (Fig. 1e), in agreement with the SST estimates from marine sediment core MD01-2444⁴⁰.

These deglacial changes are interrupted by HS11, during which a weakened AMOC²⁹ induces a ~1° SST decrease in the North Atlantic compared to the penultimate glacial maximum (PGM, here taken at 140 ka). At the end of HS11, the AMOC resumption leads to an abrupt warming in the North Atlantic region as well as an increase in precipitation over southern Europe in agreement with paleo-records (Fig. 1c, e, f)^{40–43}. The simulated end of HS11 is coeval with the increase in atmospheric CH₄⁴⁴ and the increase in precipitation over southern Europe⁴⁰ (Fig. 1b, f).

At the PGM, the simulated precipitation is low across tropical north Africa (≤ 20 cm.yr⁻¹, Figs. 1g, h and 2a, b). As a result, the desert dominates tropical north Africa between ~16°N and 32°N and reaches 8°N in the east (Fig. 2c, d). An abrupt increase in precipitation is observed at the end of HS11, with a maximum reached at ~128.4 ka (Figs. 1g, h and 2a, b).

The simulated precipitation evolution is in good agreement with an Al/Si record (Fig. 1h, green) obtained from marine sediment core GeoB7925-1 from the western African margin, and which provides an estimate of runoff from the western part of the Sahara²⁰. The initially published age model of this core²⁰ was revised here using the radiometrically-dated time scale of speleothems from Corchia Cave^{40,45}, in order to match the latest chronological improvements proposed for Termination II and the LIG³⁸. This record suggests very dry conditions during HS11,

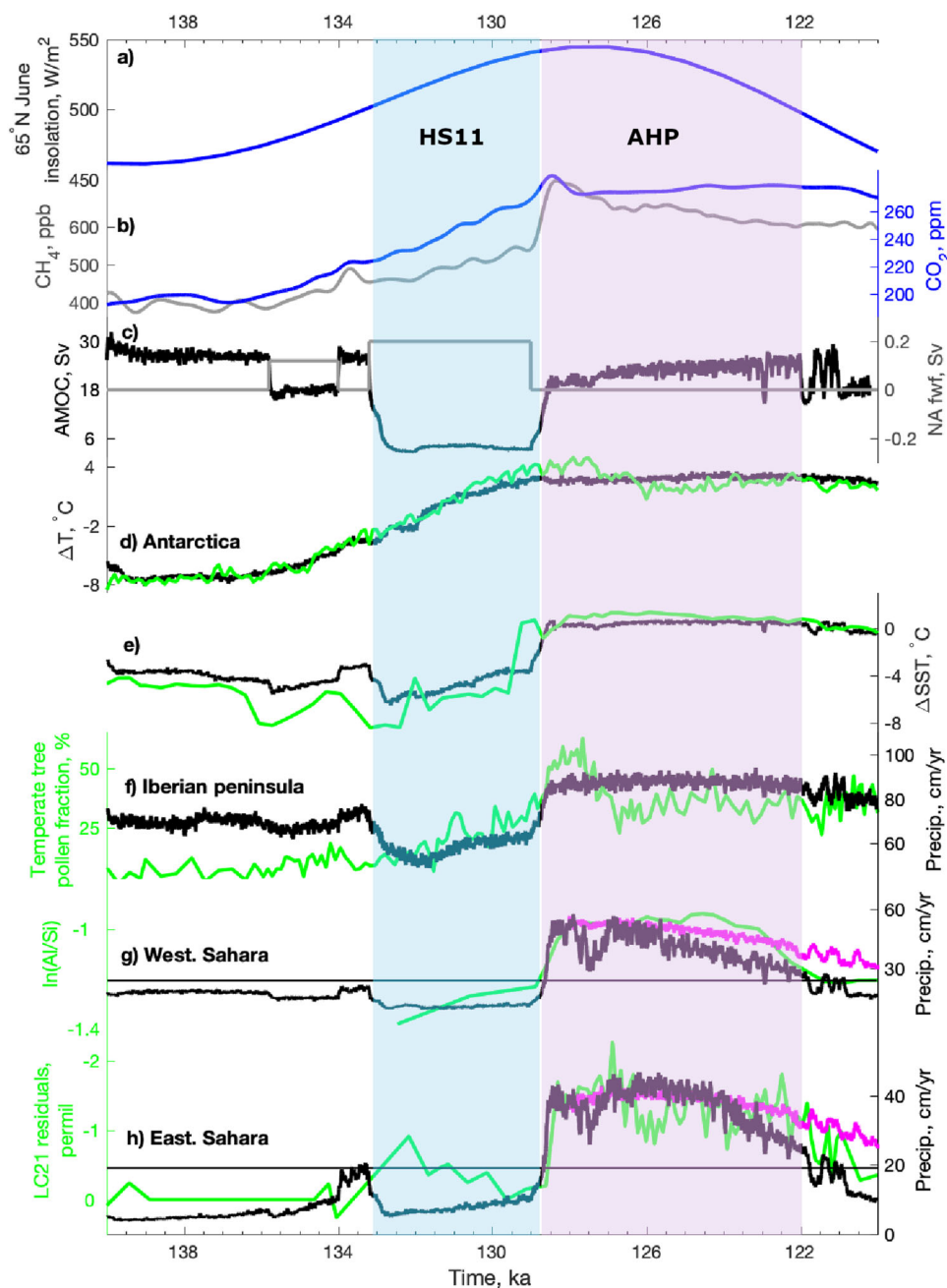


Fig. 1 Overview of the penultimate deglaciation and LIG. Main forcing and results of the transient *Full* experiment (black) compared to key paleo-records (green). Time series of **a** 65°N June insolation³⁶; **b** atmospheric CO₂ (blue) and CH₄ (grey) as measured in the EDC ice core^{37, 44, 70} on the AICC2012 chronology⁷³ used as forcing for the transient experiments. Time series of **c** North Atlantic meltwater forcing (grey), and simulated AMOC (black); **d** Annual mean Antarctic (75°S–90°S) air temperature anomalies compared to the temperature estimate from the EDC ice core³⁹ on the AICC2012 chronology; **e** Annual mean Iberian margin (15°W–8°W, 37°N–43°N) SST anomalies compared to UK₃₇ derived SST from marine sediment core MD01-2444⁴⁰; **f** Annual mean precipitation on the Iberian Peninsula compared to the temperate tree pollen fraction (%) from joint marine-terrestrial analyses of the MD01-2444 deep-sea core⁴⁰; **g** Annual mean precipitation over northwest Africa (20°W–0°W, 15°N–30°N) in *Full* (black), *VegLIG* (magenta) and *PI* (horizontal thin black), compared to ln(AI/Si) record in GeoB7925-1 (green) indicating runoff from northwest Africa²⁰; **h** Annual mean precipitation over northeast Africa (15°E–32°E, 15°N–30°N) in *Full* (black), *VegLIG* (magenta) and *PI* (horizontal thin black), compared to LC21 residuals (green) as a proxy for runoff from northeast Africa²². Blue shading indicates the main part of HS11 and purple shading corresponds to the AHP.

followed by an increase in precipitation and peak wet conditions at ~127 ka lasting until ~124 ka. The AI/Si record then suggests a gradual return to dry conditions over the LIG. The simulated abrupt shift to wet conditions at the end of HS11 in the eastern Sahara closely follows the timing of African monsoon runoff as derived from a planktic $\delta^{18}\text{O}$ residual record from the Mediterranean Sea core LC21²² (Fig. 1h, green).

Both the extent and intensity of the WAM are stronger during the LIG between 128.6 and 122 ka than during PI, with a $\sim 2.5 \text{ mm.d}^{-1}$ precipitation increase over the Sahara, extending across the Arabian peninsula (Fig. 3a, c). The simulated LIG WAM lasts from June to September over the Sahel, and from mid-June to September over the Sahara, but the coastal Mediterranean region in North Africa also receives increased

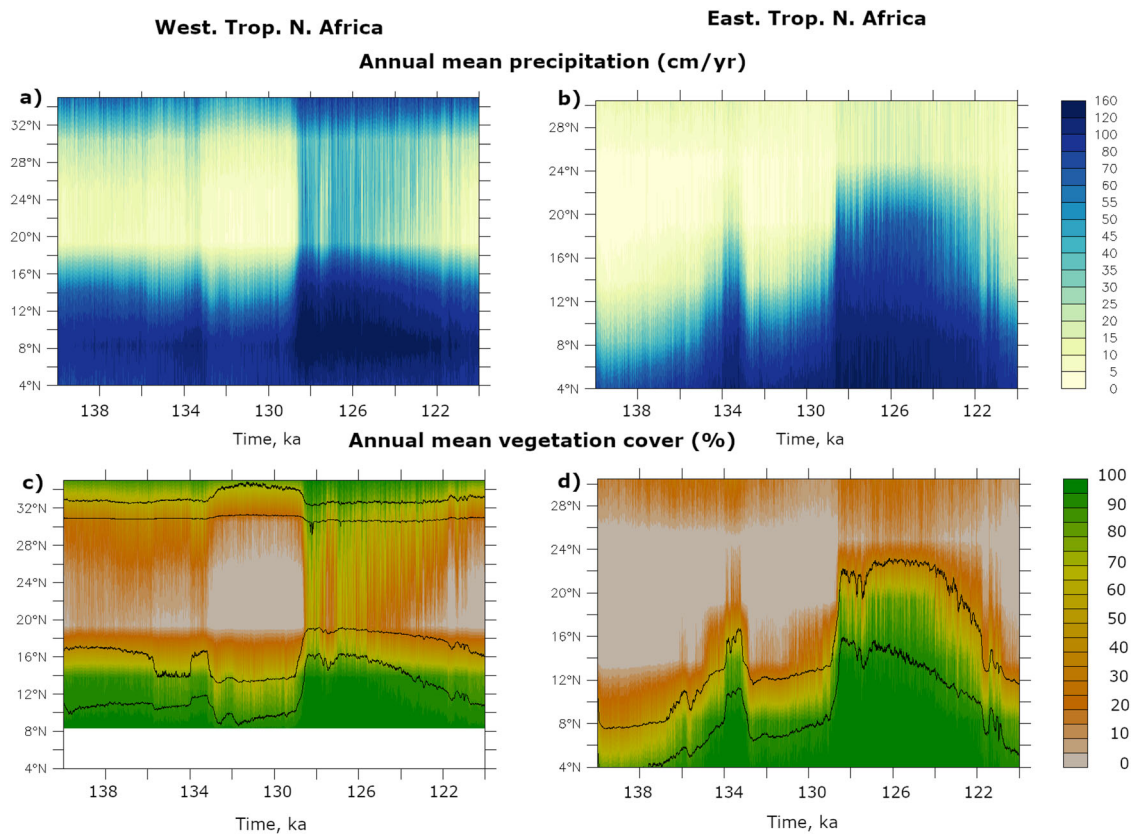


Fig. 2 Precipitation and vegetation cover evolution across tropical north Africa. Hovmöller diagrams of annual mean **a, b** precipitation ($\text{cm}\cdot\text{yr}^{-1}$) and **c, d** vegetation cover (%) averaged over **a, c** northwestern ($20^{\circ}\text{W}-0^{\circ}$) and **b, d** northeastern ($15^{\circ}\text{E}-30^{\circ}\text{E}$) Africa as a function of latitude and across the penultimate deglaciation and LIG (140 to 120 ka). The 25 and 5% tree lines are shown with a black solid line in **c, d**. Note the different y-axis for the western and eastern parts, reflecting the different latitudinal land boundary conditions.

precipitation in autumn from a southwesterly flow, and weaker anticyclonic circulation over the Azores (Supplementary Fig. 1). As a result, annual mean precipitation is higher over tropical north Africa and the Arabian peninsula by $\sim 35 \text{ cm}\cdot\text{yr}^{-1}$ at the LIG, in line with proxy records⁴⁶ (Supplementary Fig. 2).

The increase in precipitation at the end of the penultimate deglaciation induces an expansion of vegetation across tropical north Africa and into the Sahara (Figs. 2c, d and 3a, g). This simulation thus suggests a ‘green Sahara’, with the total fraction of grass plus trees generally above 50% between ~ 128.6 and 124 ka. These vegetation changes impact surface albedo, which is ~ 0.1 to 0.15 lower between 15°N and 30°N at 128 ka than during PI (Fig. 3d–f). The vegetation-albedo feedback contributes to the high LIG precipitation: if vegetation distribution, and thus also albedo, are kept at their PI level, precipitation over the Sahara is 40% lower (Supplementary Table 1). Changes in albedo alter the radiative balance, and therefore the upward motion of air above the Sahara. The lower LIG albedo thus reduces subsidence^{47,48}.

Due to the summer monsoon precipitation, and coastal precipitation in autumn (Supplementary Fig. 1), the simulated vegetation cover over the western part of tropical Africa is $\sim 70\%$, with the 5% tree fraction reaching 18°N between 128.6 and 125.6 ka (Figs. 2c and 3g). Due to a slightly expanded northward incursion of the monsoonal flow, and autumn precipitation on the Mediterranean coast, a vegetated corridor is simulated at $5^{\circ}\text{W}-10^{\circ}\text{E}$ between 128.6 and 125.6 ka (Fig. 3g). On the eastern part, while desert still dominates north of 22°N throughout the LIG, between 128.6 and 124 ka precipitation is high and vegetation cover is close to 100% south of 20°N , with the 5% tree fraction also reaching 22°N (Figs. 2d and 3g). An abrupt 19%

drop in precipitation and vegetation cover occurs over western tropical north Africa at 125.6 ka, while there is no change in the northeast (Figs. 1g, h and 2). This abrupt change is not due to an AMOC weakening and is not simulated if the vegetation cover is fixed at 128 ka level (Fig. 1g, magenta), highlighting the role of the insolation decrease leading to a vegetation-albedo feedback⁴⁹. The precipitation decrease reduces the vegetation cover, which leads to an albedo increase (Supplementary Fig. 3). This alters the radiative balance, thus decreasing surface air temperature over that region, and impacting the atmospheric circulation (Supplementary Fig. 4). Precipitation and vegetation cover then further gradually decrease in the northwest, until dropping below PI levels during a centennial-scale AMOC weakening at 122 ka (Figs. 1g and 2). In the eastern part of tropical north Africa precipitation stays at its maximum level until 124 ka, after which it decreases sharply, and drops below PI levels at 122 ka (Fig. 1h). Similar to the abrupt drying at 125.6 ka in the northwest, the 124 ka drying event in the northeast arises from vegetation-albedo feedback due to the insolation decrease, as it is not simulated when vegetation is fixed at 128 ka (Fig. 1h, magenta line and Supplementary Figs. 4, 5).

Drivers of precipitation changes over tropical north Africa at the end of the deglaciation. The low precession, and associated high boreal summer insolation, lead to a high tropical Atlantic meridional SST gradient ($\sim 0.7^{\circ}\text{C}$, $5^{\circ}\text{N}-30^{\circ}\text{N}$ compared to $30^{\circ}\text{S}-5^{\circ}\text{N}$ ⁵⁰), and a northward shift of the ITCZ over the Atlantic during the early LIG (Fig. 3a and Supplementary Table 1). The low-level westerly flow associated with the WAM reaches 23°N at the LIG, and the Sahara heat low is strong (Supplementary Fig. 6).

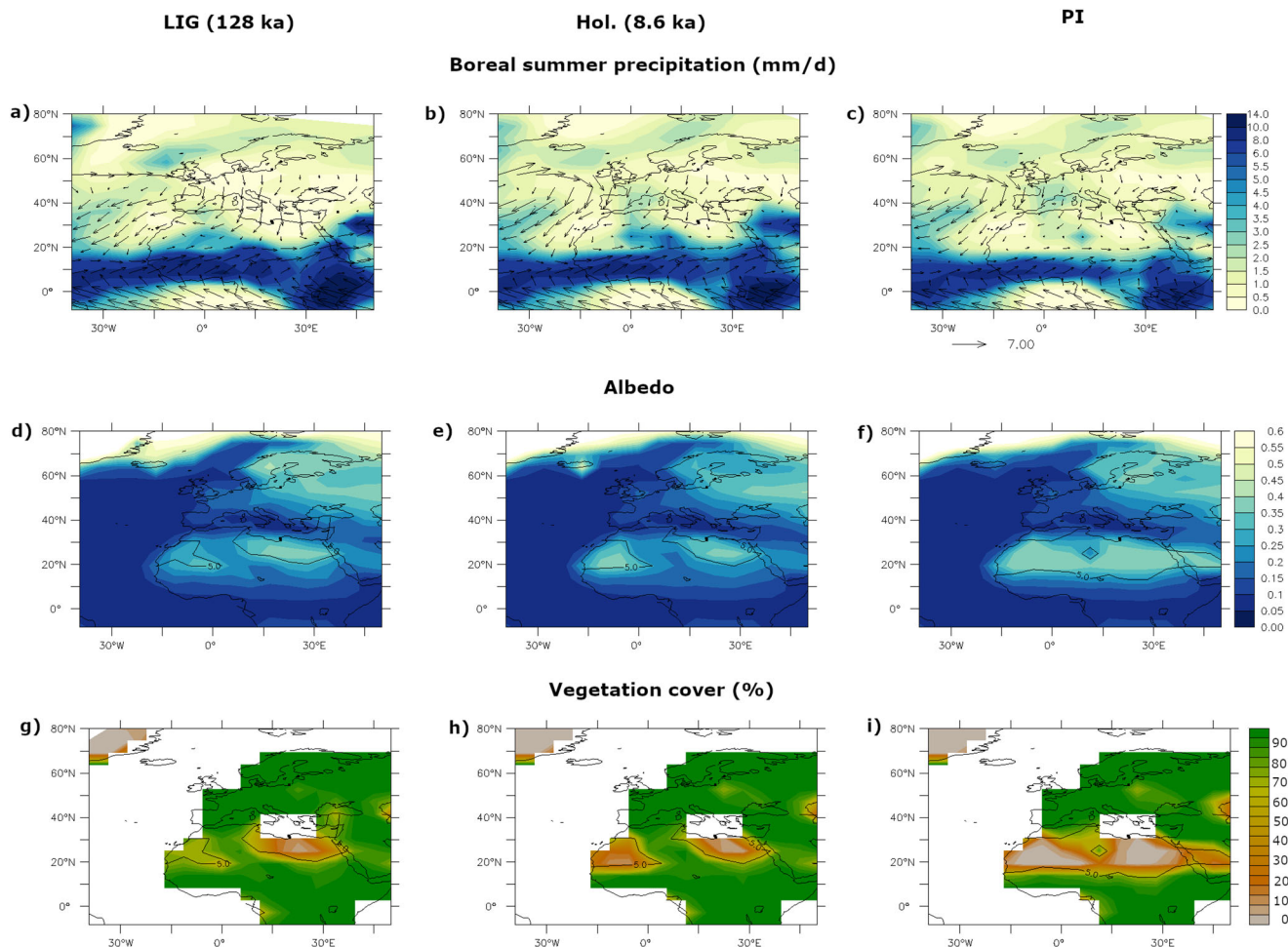


Fig. 3 Precipitation, albedo and vegetation cover during the LIG, mid-Holocene and PI. **a–c** Boreal summer precipitation ($\text{mm}\cdot\text{d}^{-1}$, shading) and 800 mb winds ($\text{m}\cdot\text{s}^{-1}$, vector), **d–f** Annual mean surface albedo and **g–i** vegetation cover (%), grass plus tree fractions) during (left) the LIG (128 ka), (middle) the mid-Holocene (8.6 ka) and (right) PI. The 5% tree fraction contour line (black) is also included over northern Africa and the Middle East in the albedo and vegetation cover plots.

The AEJ is also displaced northward, reaching $\sim 25^\circ\text{N}$ (Supplementary Fig. 7).

To constrain the processes that control the initiation, demise and amplitude of the AHP at the LIG, a set of transient sensitivity simulations is performed with forcings each in turn fixed at 140 ka levels (Methods). Figures 4a and 5 clearly highlight that high boreal summer insolation, brought about by low precession, primarily controls the emergence and amplitude of precipitation over tropical north Africa. When orbital parameters are fixed at 140 ka (*FixOrb*), precipitation over the Sahel and Sahara is reduced by ~ 40 and $\sim 70\%$, respectively compared to the *Full* experiment (Fig. 4a). Figure 5a also shows that for positive precession values, which correspond to June insolation at 65°N below $\sim 500 \text{ W m}^{-2}$, precipitation over tropical north Africa is suppressed. Changes in insolation impact the tropical Atlantic SST gradient, which modulates the position of the ITCZ⁵⁰. The tropical SST gradient is 60% larger in *Full* compared to *FixOrb* (Fig. 4i and Supplementary Table 1), which strengthens the summer ITCZ and shifts its location 4° northward, thus enhancing precipitation over tropical north Africa and in particular over the Sahara. In addition, the Sahara heat low is much weaker in *FixOrb* than in *Full*, and the AEJ is displaced 2° southward, thus leading to a weaker WAM in *FixOrb*^{4,6} (Fig. 4e and Supplementary Fig. 7).

At high precession (≥ 0), i.e. low NH boreal summer insolation (Fig. 5), precipitation over tropical north Africa is low and displays reduced variability: the possible full range of precipitation level is $\leq 30 \text{ cm}\cdot\text{yr}^{-1}$. As precession decreases (and thus NH insolation increases), the range of possible precipitation over tropical north Africa increases, with a maximum range of over $50 \text{ cm}\cdot\text{yr}^{-1}$ at the peak of insolation (Fig. 5a). Most of this variability is due to changes in AMOC strength: if the AMOC is weak, precipitation is suppressed over the Sahara and very low over the Sahel irrespective of NH summer insolation level (Figs. 4b and 5). At high insolation levels, the AMOC modulates the precipitation over tropical north Africa, with the potential to reduce it by $\sim 75\%$ over the Sahara and $\sim 45\%$ over the Sahel, an effect that is comparable to changes in insolation (Fig. 4a, b). The reduced meridional oceanic heat transport to the North Atlantic when the AMOC is weak leads to a cooling of the North Atlantic, while the tropical South Atlantic warms (Fig. 4j). This induces a reversed tropical Atlantic SST gradient and a southward shift of the ITCZ^{32,51} (Supplementary Table 1). The southward shift of the ITCZ and weaker WAM lead to dry conditions over tropical north Africa, with a stronger impact over western than eastern Sahara. In addition, a weak AMOC also leads to a more southward position of the AEJ (Supplementary Fig. 7), which would further reduce precipitation over northern Africa. As

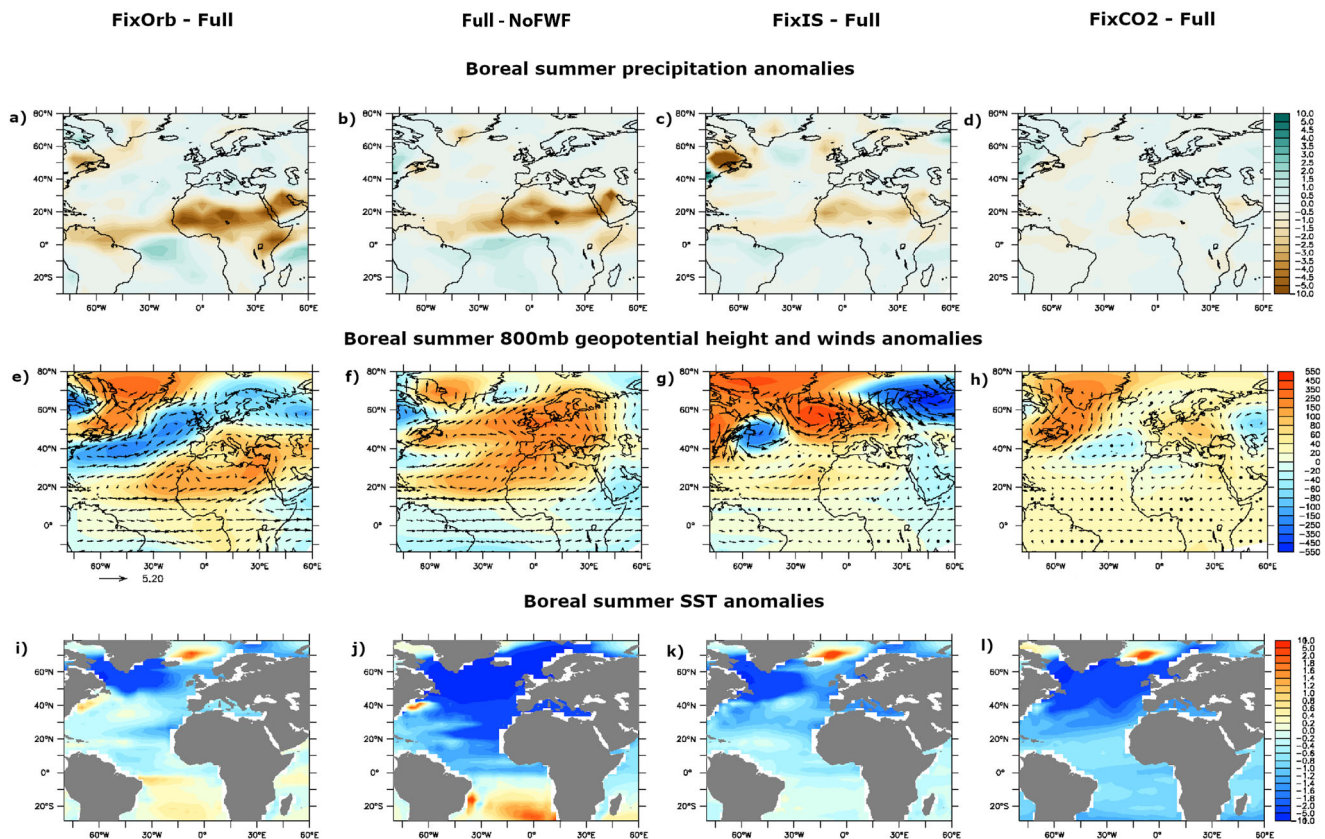


Fig. 4 Processes driving the AHP. (top) Boreal summer **a–d** precipitation anomalies ($\text{mm}\cdot\text{d}^{-1}$); (middle) **e–h** 800 mb geopotential height and wind anomalies (hPa and m/s); (bottom) **i–l** SST anomalies ($^{\circ}\text{C}$) for simulations **a, e, i** *FixOrb*, **b, f, j** *Full* at 129 ka with a weak AMOC compared to *noFWF* at 129 ka, **c, g, k** *FixIS* and **d, h, l** *FixCO2* compared to *Full* at 128 ka.

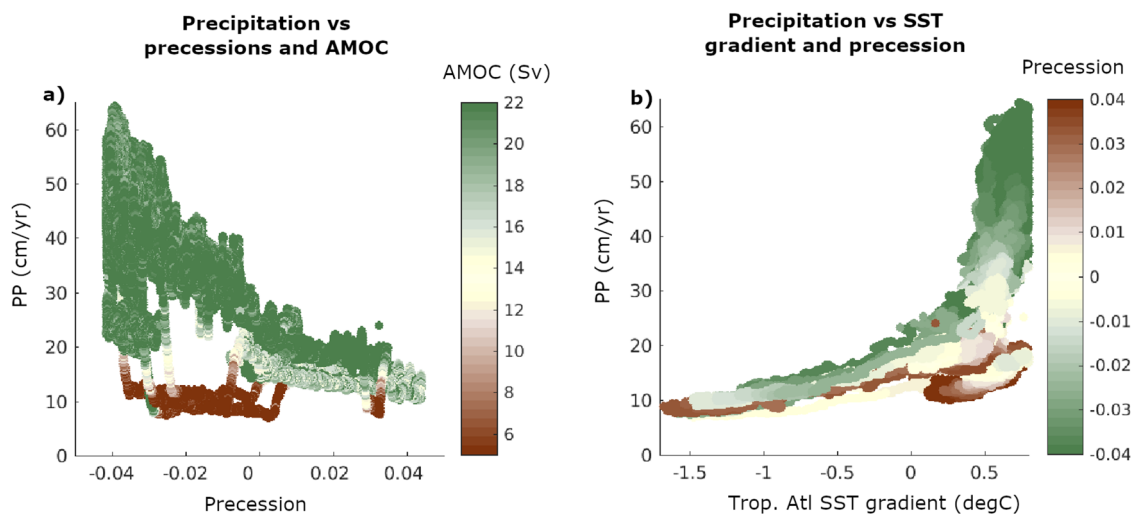


Fig. 5 Drivers of precipitation changes over tropical north Africa. Annual mean precipitation over western tropical north Africa ($20^{\circ}\text{W}-0^{\circ}$, $15^{\circ}\text{N}-30^{\circ}\text{N}$) as a function of **a** precession with symbols shading representing the strength of the AMOC (Sv) and **b** the tropical Atlantic meridional SST gradient ($^{\circ}\text{C}$, $70^{\circ}\text{W}-20^{\circ}\text{W}$, $5^{\circ}\text{N}-30^{\circ}\text{N}$ compared to $40^{\circ}\text{W}-5^{\circ}\text{E}$, $30^{\circ}\text{S}-5^{\circ}\text{N}$ ⁵⁰) with symbols shading representing precession, for simulations *Full*, *FixIS*, *FixCO2* and *NoFWF*.

millennial-scale AMOC weakenings are a common feature of deglaciations, this implies that the AMOC recovery at the end of these events controls the initiation of AHPs during the following interglacials. However, AMOC impacts are not restricted to deglaciations, and centennial-scale periods of AMOC weakening have been evidenced during the LIG^{40,52}. The full transient simulation presented here indeed displays some episodes of

AMOC weakening, which lead to abrupt drying of tropical north Africa, with an expansion of desert towards the end of the AHP (e.g. at 121. ka) (Figs. 1g, h and 2). AMOC variations could thus also trigger the demise of the AHP during the LIG.

Figure 5a shows that changes in precession and AMOC do not explain everything, as even for low precession and a strong AMOC precipitation can be relatively low over tropical north

Africa (e.g. 20–30 cm.yr⁻¹ for precession ≤ -0.03 and AMOC ≥ 22 Sv). While secondary to insolation and AMOC, the presence of glacial ice-sheets over NH land masses impacts tropical hydrology as they lead to a more southward position of the ITCZ ($\sim 3^\circ$ southward in *FixIS*) compared to the *Full* simulation (Fig. 4c and Supplementary Table 1). Through the albedo feedback, the extended NH ice sheets lower NH temperature, maintain cold conditions in the North Atlantic and a weak tropical SST gradient (Fig. 4k and Supplementary Table 1). The large Laurentide ice-sheet also creates a positive geopotential height anomaly centred on the North Atlantic, which extends to the northwest of Africa (Fig. 4g). This induces $\sim 1^\circ\text{C}$ colder conditions over northwest Africa maintaining a weaker WAM compared to *Full*. In addition, this weaker meridional temperature gradient over northern Africa leads to a $\sim 3^\circ$ southward shift of the AEJ compared to *Full*, which would also contribute to lower precipitation over tropical north Africa (Supplementary Fig. 7). As a result, the transient simulation in which NH ice sheets are kept at their 140 ka size (*FixIS*) displays 55 and 45% lower precipitation over northwestern and northeastern Africa, respectively during the LIG compared to the *Full* simulation (Fig. 4c and Supplementary Table 1).

While the deglacial increase in atmospheric CO₂ plays a dominant role in the deglacial temperature increase (Fig. 4l), it impacts the WAM only marginally (5 to 12%) as it does not significantly affect the tropical Atlantic SST gradient nor the meridional air temperature gradient over tropical north Africa (Fig. 4d and Supplementary Table 1).

Comparison with the last deglaciation. A comparison of the precipitation evolution over tropical north Africa across the penultimate deglaciation with results from a transient simulation of the last deglaciation previously performed with LOVECLIM⁵³ (Methods) supports our conclusions (Fig. 6). Due to the stronger insolation forcing, and the AMOC reaching a maximum strength concurrently with the end of the demise of the NH glacial ice-sheets, the simulated precipitation increase over tropical north Africa is larger and more abrupt during the penultimate than the last deglaciation, particularly in the west due to the NH ice-sheet impact. An increase in precipitation and vegetation advance is simulated during the Bølling–Allerød (~ 14.7 – 13 ka), as this corresponds to a period of relatively high NH summer insolation (~ 510 W.m⁻²) and strong AMOC (Fig. 6). However, the precipitation increase over the Sahara is small and does not reach PI levels because of the large NH ice sheets still present at the time. Despite the boreal summer insolation being close to its maximum level during the AMOC recovery at the end of the Younger Dryas (here at ~ 11.7 ka), $\sim 30\%$ of the NH glacial ice-sheets are still present^{54,55} (Fig. 6b), thus attenuating the precipitation increase over tropical north Africa. The disintegration of NH ice sheets during the early Holocene thus leads to a further increase in precipitation over tropical north Africa until 8.7 ka.

The stronger summer insolation forcing at high northern latitudes leads to much wetter conditions over the western part of the Sahara during the LIG than during the Holocene (Figs. 3a, b and 6). While the desert still dominates the western Sahara during the Holocene, it features more than 50% of grass and trees during the LIG (Figs. 3g, h and 6). By contrast in northeast Africa, north of 25°N , precipitation is similar during the LIG and Holocene, and the vegetation cover is inferior to 50% during both time periods. The demise of the AHP occurs abruptly at ~ 6 ka over northeast Africa, when crossing the same insolation threshold of 0 precession (~ 500 W.m⁻²) as during the LIG at ~ 122 ka. In the northwest, precipitation gradually decreases over the Holocene to reach PI levels at ~ 5 ka.

Discussion

The experiments suggest that during the LIG the ITCZ, defined here as the latitude of maximum precipitation, was displaced northward over tropical north Africa and the WAM was stronger thus leading to higher precipitation rates over a larger area than during both the Holocene and PI (Figs. 3 and 6). While LOVECLIM does not resolve African Easterly Waves and mesoscale convective systems over tropical north Africa, these are modulated by the AEJ. A northward displacement of the AEJ is also simulated at the LIG, which would therefore contribute to enhanced precipitation over tropical north Africa¹. While the stronger WAM leads to wetter conditions over tropical north Africa in summer, the Mediterranean coast of North Africa (~ 30 – 35°N) also benefits from a 50% increase in late autumn rainfall (Supplementary Fig. 1), in agreement with CCSM3 simulations of the LIG⁵⁶ and paleo-data of the Holocene AHP^{24,57}. The simulated precipitation anomalies at the LIG compared to PI are in agreement with paleo-proxy records⁴⁶ (Supplementary Fig. 2), and are in line with results from PMIP4 equilibrium simulations of the LIG¹⁷, even if larger precipitation anomalies are simulated here north of 20°N , probably due to the vegetation-albedo feedback.

As a result of the wetter conditions during the LIG, vegetation expands over most of northern Africa, with more than $\sim 50\%$ grass cover and $\sim 10\%$ of trees over the Sahara at 128 ka, particularly along a central corridor at 0 – 10°E (Fig. 3). The simulated wetter conditions and higher vegetation cover over tropical north Africa at the LIG compared to the Holocene are consistent with paleo-environmental reconstructions¹⁰, as well as with a more intensely developed sapropel S5 compared to S1^{22,58}. Although the simulated $\sim 10\%$ tree cover over the Sahara at the peak of the LIG is an underestimation compared with a previous inference of woodland¹⁰, it is higher than in a previous study, which simulated desert between 18°N and 30°N ⁵⁶.

Under present-day conditions, the 25°C isotherm over tropical north Africa is situated at 27°N instead of 24°N in LOVECLIM, and precipitation at 30°N is overestimated³⁵. These biases could amplify the vegetation response, thus potentially leading to an overestimation of the precipitation and vegetation cover over tropical north Africa at the LIG. Previous studies focusing on LIG and mid-Holocene climate suggested that LOVECLIM's performances were on par with results from coupled general circulation models, but indeed found a strong positive precipitation-vegetation feedback over tropical north Africa^{59,60}. However, recent mid-Holocene sensitivity experiments studying the impact of land surface and albedo changes on tropical north African precipitation support our simulated albedo and precipitation changes as well as the northward shift of the AEJ^{25,61}. In addition, simulated precipitation and vegetation cover in LOVECLIM during the LIG and mid-Holocene are in agreement with proxy records^{24,46}.

Our transient experiments support an abrupt initiation of the AHP during the penultimate deglaciation, while the AHP initiation was more gradual during the last deglaciation, particularly in the Western Sahara. While their timings broadly follow NH insolation, their initiation is determined by the AMOC strengthening at the end of deglacial millennial-scale events. To second order, the disintegration of NH ice sheets also impacts the initiation of the AHP, through warming of the North Atlantic and changes in atmospheric circulation⁶².

Based on the AMOC and NH ice-sheet scenarios presented here, the precipitation maximum over tropical north Africa is simulated at 128.4 ka, thus 1.4 kyr before the insolation peak at the LIG, while during the Holocene the maximum is reached at 9.8 ka in the northeast but only at 8.7 ka in the northwest, thus 1.2 to 2.3 kyr after the insolation peak of the Holocene. With respect

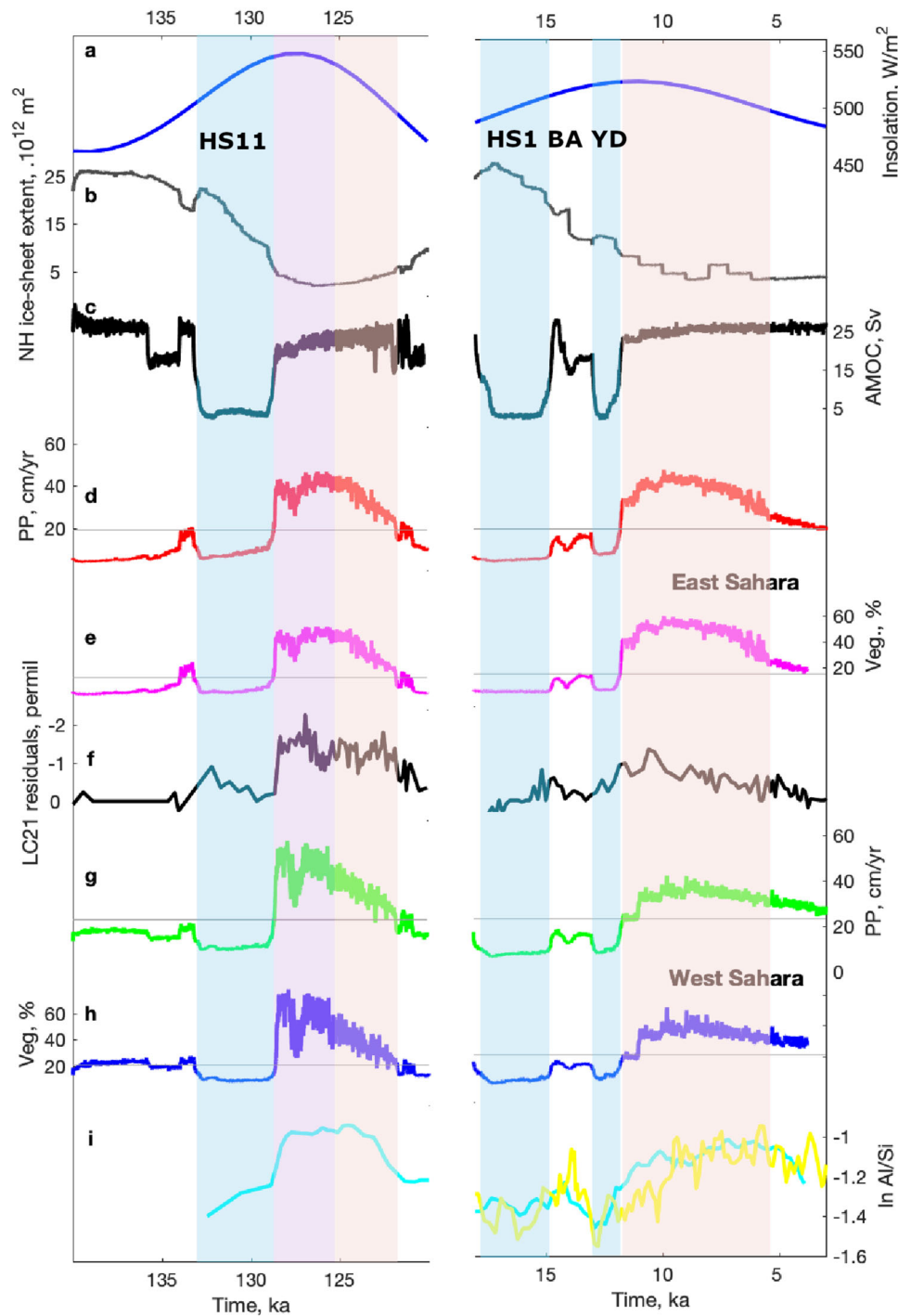


Fig. 6 Comparison between the penultimate and last deglaciation. Time evolution across (left) the penultimate and (right) the last deglaciations of **a** 65°N insolation in June; **b** NH ice-sheet extent used as forcing; **c** AMOC; **d** simulated annual mean precipitation and **e** vegetation fraction over the eastern Sahara (15°N–30°N, 15°E–32°E); **f** African monsoon runoff estimate from Mediterranean Sea core LC21 residuals²²; **g** simulated annual mean precipitation and **h** grass fraction over the western part of the Sahara (15°N–30°N, 20°W–0°); **i** ln Al/Si from marine sediment core GeoB7925²⁰ (cyan) and from core GeoB-7920 (yellow)^{74,75}. Blue shading represents North Atlantic cold events such as the main phase of Heinrich stadial 11 (HS11), Heinrich stadial 1 (HS1) and the Younger Dryas (YD). Pink shading represents the timing of the simulated AHP, with a particularly wet period over the western Sahara at the LIG compared to the Holocene shaded in purple. BA stands for the Bølling-Allerød. Horizontal black lines represent simulated PI values.

to insolation, the initiation of the AHP thus occurs earlier in the LIG than during the Holocene, because of the timing of the end of HS11 and the loss of NH ice-sheets. The presence of NH ice sheets during the early Holocene^{54,55} indeed delays the AHP peak. The higher rate of NH summer insolation increase during the penultimate deglaciation might have induced a faster rate of

NH ice-sheets disintegration^{63–65} thus potentially leading to low NH ice-sheet volumes and strong AMOC states being reached earlier in the LIG than Holocene.

This set of simulations demonstrates that abrupt precipitation transitions in tropical north Africa as a response to slow insolation changes are possible. These abrupt transitions can be

triggered by AMOC changes, vegetation-albedo feedbacks, and changes in NH ice-sheets extent. However, these mostly occur for negative precession values, i.e. high northern latitude summer insolation values above $\sim 500 \text{ W.m}^{-2}$. The background state thus conditions the capacity to generate abrupt changes, with higher insolation values associated with a higher potential of change. The background state also leads to zonal and meridional timing differences in abrupt shifts to drier conditions across tropical north Africa.

Some abrupt changes in precipitation and vegetation are simulated during both the LIG and Holocene, even though the variability is larger during the LIG than the Holocene. The larger LIG variability is due to the wetter background conditions, particularly in northwest Africa, as well as to the larger AMOC variability. It has been shown that the LIG was punctuated by centennial-scale AMOC weakening events⁴⁰, which could have also led to an abrupt weakening of the WAM and abrupt return to arid conditions over the Sahara.

Whether rainfall over tropical north Africa will increase or decrease over the coming century is highly debated. The experiments performed here suggest a slightly stronger WAM with increasing atmospheric CO_2 . However, our simulations highlight the dominant role of the AMOC and orbital parameters in setting the positions of the ITCZ and AEJ, and impacting precipitation over tropical north Africa. As precession is positive, and as the AMOC is projected to slow down by $\sim 40\%$ over the coming century⁶⁶ without taking into account enhanced Greenland runoff⁶⁷, an increase in rainfall over tropical north Africa appears unlikely.

Methods

A transient simulation covering the penultimate deglaciation and the last interglacial period (140 to 120 ka) is performed with the Earth system model LOVECLIM³⁵. LOVECLIM comprises an ocean general circulation model ($3^\circ \times 3^\circ$, 20 vertical levels), coupled to a dynamic-thermodynamic sea-ice model, a quasi-geostrophic T21 atmospheric model, a vegetation model and a global carbon cycle model. The vegetation model includes two plant functional types: trees and grasses. The vegetation fraction is the sum of the tree and grass fractions. The vegetation fraction is a function of growing degree-days above 0°C and annual mean precipitation. Vegetation changes impact the surface albedo, but not evapotranspiration.

The transient simulation (*Full*) follows the PMIP4 protocol described in ref. ³⁸. The model is first integrated to equilibrium under 140 ka boundary conditions, with appropriate orbital parameters, greenhouse gas content (CO_2 of 191 ppm, CH_4 of 385 ppb and N_2O of 201 ppb), and continental ice-sheet geometry and albedo^{38,55,68,69}. LOVECLIM is then run from 140 to 120 ka with varying orbital parameters, greenhouse gas content^{37,70} and continental ice-sheet geometry and albedo^{38,55,68,69}. The Bering Strait is gradually opened between 132 and 131.8 ka. To simulate the impact of the deglacial ice-sheet disintegration and associated sea-level rise, meltwater is added into the North Atlantic (50°N – 60°N , 60°W – 10°W). This meltwater input is a simplified version of scenario fIRD, which is based on the time evolution of IRD input into the North Atlantic³⁸. As shown in Fig. 1c, 0.12 Sv is added between 135.8 and 134 ka (sea-level equivalent (s.l.e.) of 19.2 m), and 0.2 Sv is added between 133.2 and 129 ka (s.l.e. of 74.8 m). The main difference with scenario fIRD is that the meltwater flux here stops at 129 ka instead of 129.2 ka in fIRD.

To disentangle the impacts of deglacial changes in insolation, northern hemispheric ice-sheet, greenhouse gases and meltwater input, additional transient deglacial simulations are performed. Since there are little changes in most of the forcings, and little climatic variability between 140 and 134 ka (Fig. 1), the sensitivity experiments only start at 134 ka from *Full*, and each forcing is in turn fixed at its 140 ka level: orbital parameters are fixed at 140 ka in *FixOrb*, NH ice-sheets are fixed at 140 ka in *FixIS*, atmospheric CO_2 is fixed at 190 ppm in *FixCO2*, and no meltwater is added in *NoFWF*. Additional experiments were also performed to isolate the impact of vegetation changes. A LIG experiment was run with vegetation fixed at PI level (*VegPI*), and another one (*VegLIG*) was run from 128 to 120 ka with vegetation fixed at 128 ka.

The seasonal data has been adjusted following Bartlein et al., 2019⁷¹ and using 20 years of daily outputs at 128 ka.

The transient simulation of the last deglaciation is described in detail in Menviel et al. (2011)⁵³, and similar to the transient simulation of the penultimate deglaciation was forced by the time evolution of orbital parameters, northern hemispheric ice-sheet topography and albedo, greenhouse gases and meltwater input into the North Atlantic. This meltwater input was designed to produce a climatic

evolution in relative agreement with Greenland ice core GISP2 surface air temperature evolution⁷². In the North Atlantic, 0.2 Sv was added between 18 and 17.4 ka, and 0.25 Sv between 17.4 and 15.6 ka to represent Heinrich stadial 1. For the Older Dryas period, 0.2 to 0.25 Sv was added between 14.4 and 13 ka. Finally, 0.25 Sv is applied in the Arctic Ocean (175°W – 95°W , 67°N – 83°N) between 13 and 12.2 ka to mimic the Younger Dryas.

Data availability

The modelling data is available from Research Data Australia <https://doi.org/10.26190/kewt-qg48>.

Code availability

The transient experiments were performed with the Earth system model LOVECLIM. LOVECLIM can be freely downloaded from the website of the Université Catholique de Louvain: <https://www.elic.ucl.ac.be/mods/index.php?id=81>.

Received: 7 July 2021; Accepted: 28 October 2021;

Published online: 18 November 2021

References

- Nicholson, S. The west African Sahel: a review of recent studies on the rainfall regime and its interannual variability. *ISRN Meteorology* **2013**, 32 <https://doi.org/10.1155/2013/453521> (2013). Article ID 453521.
- Schneider, T., Bischoff, T. & Haug, G. Migrations and dynamics of the intertropical convergence zone. *Nature* **513**, 45–53 (2014).
- Cook, K. H. Generation of the African easterly jet and its role in determining West African precipitation. *J. Clim.* **12**, 1165–1184 (1999).
- Nicholson, S. E. & Grist, J. P. The seasonal evolution of the atmospheric circulation over West Africa and equatorial Africa. *J. Clim.* **16**, 1013–1030 (2003).
- Thorncroft, C. D. & Blackburn, M. Maintenance of the African easterly jet. *Q. J. R. Meteorol. Soc.* **125**, 763–786 (1999).
- Nicholson, S. E. A revised picture of the structure of the monsoon and land ITCZ over West Africa. *Clim. Dyn.* **32**, 1155–1171 (2009).
- Watrin, J., Lézine, A.-M. & Hély, C. Plant migration and plant communities at the time of the green sahara. *Comptes Rendus Geosci.* **341**, 656–670 (2009).
- Drake, N. A., Blench, R. M., Armitage, S. J., Bristow, C. S. & White, K. H. Ancient watercourses and biogeography of the Sahara explain the peopling of the desert. *Proc. Natl Acad. Sci. USA* **108**, 458–462 (2011).
- Ziegler, M., Tuenter, E. & Lourens, L. The precession phase of the boreal summer monsoon as viewed from the eastern Mediterranean (ODP Site 968). *Quat. Sci. Rev.* **29**, 1481–1490 (2010).
- Larrasoana, J. C., Roberts, A. P. & Rohling, E. J. Dynamics of green Sahara periods and their role in hominin evolution. *PLoS ONE* **8**, e76514 (2013).
- Brierley, C., Manning, K. & Maslin, M. Pastoralism may have delayed the end of the green Sahara. *Nat. Commun.* **9**, 4018 <https://doi.org/10.1038/s41467-018-06321-y> (2018).
- Pausata, F. S. et al. The greening of the Sahara: past changes and future implications. *One Earth* **2**, 235–250 (2020).
- Blanchet, C. et al. Drivers of river reactivation in North Africa during the last glacial cycle. *Nat. Geosci.* **14**, 97–103 (2021).
- Past Interglacials Working Group of PAGES. Interglacials of the last 800,000 years. *Rev. Geophys.* **54**, 162–219 (2016).
- Capron, E., Govin, A., Feng, R., Otto-Bliesner, B. & Wolff, E. Critical evaluation of climate syntheses to benchmark CMIP6/PMIP4 127 ka Last Interglacial simulations in the high-latitude regions. *Quat. Sci. Rev.* **168**, 137–150 (2017).
- Hoffman, J., Clark, P., Parnell, A. & He, F. Regional and global sea-surface temperatures during the last interglaciation. *Science* **355**, 276–279 (2017).
- Otto-Bliesner, B. L. et al. Large-scale features of last interglacial climate: results from evaluating the *lig127k* simulations for CMIP6-PMIP4. *Clim. Past* **17**, 63–94 (2021).
- Castañeda, I. S. et al. Wet phases in the Sahara/Sahel region and human migration patterns in North Africa. *Proc. Natl Acad. Sci. USA* **106**, 20159–20163 (2009).
- Dupont, L. Orbital scale vegetation change in Africa. *Quat. Sci. Rev.* **30**, 3589–3602 (2011).
- Govin, A., Varma, V. & Prange, M. Astronomically forced variations in western African rainfall (21°N – 20°S) during the last interglacial period. *Geophys. Res. Lett.* **41**, 2117–2125 (2014).
- Rohling, E. et al. African monsoon variability during the previous interglacial maximum. *Earth Planet. Sci. Lett.* **202**, 61–75 (2002).
- Grant, K. et al. The timing of Mediterranean sapropel deposition relative to insolation, sea-level and African monsoon changes. *Quat. Sci. Rev.* **140**, 125–141 (2016).

23. Braconnot, P., Joussaume, S., Marti, O. & de Noblet, N. Synergistic feedbacks from ocean and vegetation on the African monsoon response to mid-Holocene insolation. *Geophys. Res. Lett.* **26**, 2481–2484 (1999).
24. Tierney, J. E., Pausata, F. S. & deMenocal, P. B. Rainfall regimes of the Green Sahara. *Sci. Adv.* **3**, e1601503 (2017).
25. Chandan, D. & Peltier, W. African humid period precipitation sustained by robust vegetation, soil, and lake feedbacks. *Geophys. Res. Lett.* **47**, e2020GL088728 (2020).
26. Singarayer, J. S. & Burrough, S. L. Interhemispheric dynamics of the African rainbelt during the late quaternary. *Quat. Sci. Rev.* **124**, 48–67 (2015).
27. Heinrich, H. Origin and consequences of cyclic ice rafting in the northeast Atlantic Ocean during the past 130,000 years. *Quat. Res.* **29**, 142–152 (1988).
28. McManus, J. F., Francois, R., Gherardi, J. M., Keigwin, L. D. & Brown-Leger, S. Collapse and rapid resumption of Atlantic meridional circulation linked to deglacial climate changes. *Nature* **428**, 834–837 (2004).
29. Böhm, E. et al. Strong and deep Atlantic meridional overturning circulation during the last glacial cycle. *Nature* **517**, 73–76 (2015).
30. Stouffer, R., Seidov, D. & Haupt, B. Climate response to external sources of freshwater: North Atlantic versus the Southern Ocean. *J. Clim.* **20**, 436–448 (2007).
31. Tjallingii, R. et al. Coherent high- and low-latitude control of the northwest African hydrological balance. *Nat. Geosci.* **1**, 670 (2008).
32. Kageyama, M. et al. Climatic impacts of fresh water hosing under last glacial maximum conditions: a multi-model study. *Clim. Past* **9**, 935–953 (2013).
33. Shanahan, T. M. et al. The time-transgressive termination of the African Humid Period. *Nat. Geosci.* **8**, 140–144 (2015).
34. Dallmeyer, A., Claussen, M., Lorenz, S. J. & Shanahan, T. The end of the African humid period as seen by a transient comprehensive Earth system model simulation of the last 8000 years. *Clim. Past* **16**, 117–140 (2020).
35. Goosse, H. et al. Description of the Earth system model of intermediate complexity LOVECLIM version 1.2. *Geosci. Model Dev.* **3**, 603–633 (2010).
36. Berger, A. Long term variations of daily insolation and quaternary climate change. *J. Atmos. Sci.* **35**, 2362–2367 (1978).
37. Köhler, P., Nehrbass-Ahles, C., Schmitt, J., Stocker, T. & Fischer, H. A 156 kyr smoothed history of the atmospheric greenhouse gases CO₂, CH₄, and N₂O and their radiative forcing. *Earth Syst. Sci. Data* **9**, 363–387 (2017).
38. Menviel, L. et al. The penultimate deglaciation: protocol for Paleoclimate Modelling Intercomparison Project (PMIP) phase 4 transient numerical simulations between 140 and 127 ka, version 1.0. *Geosci. Model Dev.* **12**, 3649–3685 (2019).
39. Jouzel, J. et al. Orbital and millennial Antarctic climate variability over the past 800,000 years. *Science* **317**, 793–796 (2007).
40. Tzedakis, P. et al. Enhanced climate instability in the North Atlantic and southern Europe during the Last Interglacial. *Nat. Commun.* **9**, 4235 (2018).
41. Chapman, M. & Shackleton, N. Millennial-scale fluctuations in North Atlantic heat flux during the last 150,000 years. *Earth Planet. Sci. Lett.* **159**, 57–70 (1998).
42. Martrat, B., Jimenez-Amat, P., Zahn, R. & Grimalt, J. Similarities and dissimilarities between the last two deglaciations and interglaciations in the North Atlantic region. *Quat. Sci. Rev.* **99**, 122–134 (2014).
43. Oppo, D., McManus, J. & Cullen, J. Evolution and demise of the Last Interglacial warmth in the subtropical North Atlantic. *Quat. Sci. Rev.* **25**, 3268–3277 (2006).
44. Loulergue, L. et al. Orbital and millennial-scale features of atmospheric CH₄ over the past 800,000 years. *Nature* **453**, 383–386 (2008).
45. Drysdale, R. et al. Magnesium in subaqueous speleothems as a potential palaeotemperature proxy. *Nat. Commun.* **11**, 5027 (2020).
46. Scussolini, P. et al. Agreement between reconstructed and modeled boreal precipitation of the Last Interglacial. *Sci. Adv.* <https://advances.sciencemag.org/content/5/11/eaax7047> (2019).
47. Charney, J. G. Dynamics of deserts and drought in the Sahel. *Q. J. R. Meteorol. Soc.* **101**, 193–202 (1975).
48. Claussen, M., Dallmeyer, A. & Bader, J. Theory and modeling of the African Humid Period and the Green Sahara. <https://oxfordre.com/climate-science/view/10.1093/acrefore/9780190228620.001.0001/acrefore-9780190228620-e-532> (2017).
49. Knorr, W. & Schnitzler, K. Enhanced albedo feedback in North Africa from possible combined vegetation and soil formation processes. *Clim. Dyn.* **26**, 55–63 (2006).
50. Biasutti, M., Held, I. M., Sobel, A. H. & Giannini, A. SST forcings and Sahel rainfall variability in simulations of the twentieth and twenty-first centuries. *J. Clim.* **21**, 3471–3486 (2008).
51. Stouffer, R. et al. Investigating the causes of the response of the thermohaline circulation to past and future climate changes. *J. Clim.* **19**, 1365–1387 (2006).
52. Galaasen, E. V. et al. Rapid reductions in north Atlantic deep water during the peak of the last interglacial period. *Science* **343**, 1129–1132 (2014).
53. Menviel, L., Timmermann, A., Timm, O. & Mouchet, A. Deconstructing the last glacial termination: the role of millennial and orbital-scale forcings. *Quat. Sci. Rev.* **30**, 1155–1172 (2011).
54. Peltier, W., Argus, D. & Drummond, R. Space geodesy constrains ice-age terminal deglaciation: the global ICE-6G-C (VM5a) model. *J. Geophys. Res. Solid Earth* **120**, 450–487 (2015).
55. Tarasov, L., Dyke, A. S., Neal, R. M. & Peltier, W. R. A data-calibrated distribution of deglacial chronologies for the North American ice complex from glaciological modeling. *Earth Planet. Sci. Lett.* **315–316**, 30–40 (2012).
56. Kutzbach, J. E. et al. African climate response to orbital and glacial forcing in 140,000-y simulation with implications for early modern human environments. *Proc. Natl Acad. Sci.* **117**, 2255–2264 (2020).
57. Cheddadi, R. et al. Early Holocene greening of the Sahara requires Mediterranean winter rainfall. *Proc. Natl Acad. Sci.* <https://www.pnas.org/content/118/23/e2024898118> (2021).
58. Konijnendijk, T., Ziegler, M. & Lourens, L. Chronological constraints on Pleistocene sapropel depositions from high-resolution geochemical records of ODP Sites 967 and 968. *Newsl. Stratigr.* **47**, 263–282 (2014).
59. Braconnot, P. et al. Results of PMIP2 coupled simulations of the mid-Holocene and last glacial maximum - Part 1: experiments and large-scale features. *Clim. Past* **3**, 261–277 (2007).
60. Nikolova, I., Yin, Q., Berger, A., Singh, U. K. & Karami, M. P. The last interglacial (Eemian) climate simulated by LOVECLIM and CCSM3. *Clim. Past* **9**, 1789–1806 (2013).
61. Gaetani, M., Messori, G., Zhang, Q., Flamant, C. & Pausata, F. S. R. Understanding the mechanisms behind the northward extension of the West African monsoon during the mid-Holocene. *J. Clim.* **30**, 7621–7642 (2017).
62. Timm, O., Köhler, P., Timmermann, A. & Menviel, L. Mechanisms for the onset of the African Humid Period and Sahara Greening 14.5–11 ka BP. *J. Clim.* **23**, 2612–2633 (2010).
63. Grant, K. et al. Rapid coupling between ice volume and polar temperature over the past 150,000 years. *Nature* **491**, 744–747 (2012).
64. Grant, K. et al. Sea-level variability over five glacial cycles. *Nat. Commun.* **5**, 5076 (2014).
65. Lambeck, K., Rouby, H., Purcell, A., Sun, Y. & Sambridge, M. Sea level and global ice volumes from the last glacial maximum to the Holocene. *Proc. Natl Acad. Sci. USA* **111**, 15296–15303 (2014).
66. Weijer, W., Cheng, W., Garuba, O. A., Hu, A. & Nadiga, B. T. CMIP6 models predict significant 21st century decline of the Atlantic meridional overturning circulation. *Geophys. Res. Lett.* **47**, e2019GL086075 (2020). [E2019GL086075](https://doi.org/10.1029/2019GL086075).
67. Goelzer, H. et al. The future sea-level contribution of the Greenland ice sheet: a multi-model ensemble study of ISMIP6. *The Cryosphere* **14**, 3071–3096 (2020).
68. Abe-Ouchi, A. et al. Insolation-driven 100,000-year glacial cycles and hysteresis of ice-sheet volume. *Nature* **500**, 190–193 (2013).
69. Briggs, R., Pollard, D. & Tarasov, L. A data-constrained large ensemble analysis of Antarctic evolution since the Eemian. *Quat. Sci. Rev.* **103**, 91–115 (2014).
70. Bereiter, B. et al. Revision of the EPICA Dome C CO₂ record from 800 to 600 kyr before present. *Geophys. Res. Lett.* **42**, 542–549 (2015).
71. Bartlein, P. J. & Shafer, S. L. Paleo calendar-effect adjustments in time-slice and transient climate-model simulations (paleocaladjust v1.0): impact and strategies for data analysis. *Geosci. Model Dev.* **12**, 3889–3913 (2019).
72. Alley, R. Ice-core evidence of abrupt climate changes. *Proc. Natl Acad. Sci. USA* **97**, 1331–1334 (2000).
73. Bazin, L. et al. An optimized multi-proxy, multi-site Antarctic ice and gas orbital chronology (AICC2012): 120–800 ka. *Clim. Past* **9**, 1715–1731 (2013).
74. Collins, J. A. et al. Interhemispheric symmetry of the tropical African rainbelt over the past 23,000 years. *Nat. Geosci.* **4**, 42–45 (2011).
75. Tjallingii, R., Röhl, U., Kölling, M. & Bickert, T. Influence of the water content on X-ray fluorescence core-scanning measurements in soft marine sediments. *Geochem. Geophys. Geosyst.* **8**, Q02004. <https://doi.org/10.1029/2006GC001393> (2007).

Acknowledgements

This project was supported by the Australian Research Council, grants FT180100606 to L.M., DP180100048 to L.M. and K.J.M. and DE190100042 to K.M.G. P.C.T. acknowledges funding from the UK Natural Environment Council (grant: NE/V001620/1). A.G. acknowledges funding from the French Research National Agency (grant ANR-18-BELM-0001-06). Experiments were performed on UNSW HPC Katana <https://doi.org/10.26190/669X-A286>. This project was facilitated by the activities of the PAGES QUIGS working group. The authors thank the reviewers for their constructive comments, which helped improve the manuscript. This is LSCE publication number 7733.

Author contributions

L.M. designed the study and performed the numerical experiments. K.M.G. contributed to the initial concept of the study and provided the data of core LC21. L.M. and A.A. analysed the simulations with help from K.J.M. A.G. adjusted the chronology and provided the data of core GeoB7925-1. L.M. wrote the manuscript with contributions from P.C.T. and all other authors. All authors contributed to the ideas in this paper.

Competing interests

The authors declare no competing interests.

Additional information

Supplementary information The online version contains supplementary material available at <https://doi.org/10.1038/s43247-021-00309-1>.

Correspondence and requests for materials should be addressed to Laurie Menviel.

Peer review information *Communications Earth & Environment* thanks Lydie Dupont and Deepak Chandan for their contribution to the peer review of this work. Primary Handling Editors: Sze Ling Ho and Joe Aslin. Peer reviewer reports are available.

Reprints and permission information is available at <http://www.nature.com/reprints>

Publisher's note Springer Nature remains neutral with regard to jurisdictional claims in published maps and institutional affiliations.



Open Access This article is licensed under a Creative Commons Attribution 4.0 International License, which permits use, sharing, adaptation, distribution and reproduction in any medium or format, as long as you give appropriate credit to the original author(s) and the source, provide a link to the Creative Commons license, and indicate if changes were made. The images or other third party material in this article are included in the article's Creative Commons license, unless indicated otherwise in a credit line to the material. If material is not included in the article's Creative Commons license and your intended use is not permitted by statutory regulation or exceeds the permitted use, you will need to obtain permission directly from the copyright holder. To view a copy of this license, visit <http://creativecommons.org/licenses/by/4.0/>.

© The Author(s) 2021